Mechanisms and consequences of intra-crystalline enrichment of ancient radiogenic Pb in detrital Hadean zircons from the Jack Hills, Western Australia

Rongfeng Ge [a, b, *], Simon A. Wilde [b], Alexander A. Nemchin [b, c], Martin J. Whitehouse [c], Jeremy J. Bellucci [c], Timmons M. Erickson [b, d]

a State Key Laboratory for Mineral Deposits Research, School of Earth Sciences and Engineering, Nanjing University, Nanjing 210093, PR China

b The Institute for Geoscience Research, School of Earth and Planetary Sciences, Curtin University, PO Box U1987, Perth, Western Australia 6845, Australia

c Department of Geosciences, Swedish Museum of Natural History, SE-104 0510 Stockholm, Sweden

d Mail Code XI3, Jacobs - JETS, Astromaterials Research and Exploration Science Division, NASA Johnson Space Center, Houston, TX 77058, USA

*Corresponding author: gerongfeng@nju.edu.cn (R. Ge)

Manuscript submitted to ***EPSL***

Abstract:

The recent discovery of Pb* (radiogenic lead) -enriched domains (PEDs) in zircon using high-resolution scanning ion imaging, atom probe tomography and transmission electron microscopy indicates that the U-Pb isotopic system in zircon can be affected not only by Pb* loss but also by intra-crystalline Pb* enrichment. However, the formation mechanism of PEDs and the consequences for *in-situ* U-Pb dating remain elusive. To further understand these issues, scanning ion imaging and U-Pb dating were carried out on 51 Hadean detrital zircon grains from the Jack Hills, Western Australia. Of these, 8 grains were found to contain micrometer-scale PEDs with elevated ^{207}Pb and ^{206}Pb in the ion images. Isotope profiles across these PEDs confirm that they represent unsupported Pb* resulting from intra-grain mobilization and local enrichment of Pb* during ancient overprinting events. The PEDs are rare in most grains, with only 1 – 3 Pb* hotspots present in any ~70 μm × 70 μm imaged area, and are located either in dark-CL, high-U growth zones, or associated with bright-CL, low-Th recrystallized domains, suggesting that they were likely formed by local-scale processes. The PEDs located in dark-CL, high-U growth zones likely resulted from Pb* trapped in local, interconnected pathways produced by radiation damage during thermal overprinting events. Those associated with bright-CL, low-Th domains are interpreted as Pb* concentrated in nanoscale pores formed during fluid-present recrystallization of non-metamict zircon. Our interpretations therefore imply that intra-crystalline enrichment of Pb* in zircon can occur at various scales and through diverse mechanisms. Age calculations based on the ion images demonstrate that incorporation of PEDs in conventional *in-situ* SIMS spots produces spuriously old ages that are either reversely discordant or concordant, depending on the time of Pb* mobilization and the analytical precision. The implication is that careful investigation of intra-grain distribution

of U-Th-Pb isotopes is required in order to better understand the U-Pb isotopic system and to obtain reliable crystallization ages for ancient zircons affected by complex Pb* mobilization and redistribution.

Keywords: Hadean; detrital zircon; Jack Hills; scanning ion imaging; unsupported radiogenic lead

Table1 . Acronyms used in this study

APT	Atom probe tomography
CL	Cathodoluminescence
EBSD	Electron backscatter diffraction
MSWD	Mean square weighted deviation
PED	Pb* (radiogenic Pb)-enriched domain
ROI	Region of interest
SHRIMP	Sensitive high-resolution ion microprobe
SII	Scanning ion imaging
SIMS	Secondary-ion mass spectrometry
TEM	Transmission electron microscopy
UHT	Ultra-high temperature

1. Introduction

Due to the absence of a rock record, our knowledge of the first half billion years of Earth history relies heavily on Hadean (≥4.0 Ga) zircon grains, the majority of which have been derived from a metaconglomerate unit in the Jack Hills supracrustal belt, Western Australia (e.g., Compston and Pidgeon, 1986). These ancient zircon grains have been extensively studied for U-Pb ages (e.g., Wilde et al., 2001; Holden et al., 2009; Valley et al., 2014; Bellucci et al., 2018), mineral inclusions (e.g., Maas et al., 1992; Hopkins et al., 2008; Rasmussen et al., 2011; Bell et al., 2015a, b), trace element compositions (e.g., Maas et al., 1992; Watson and Harrison, 2005; Trail et al., 2011), O (e.g., Valley et al., 2002; Nemchin et al., 2006) and Hf (e.g., Amelin et al., 1999; Kemp et al., 2010) isotopes, as well as paleomagnetism (e.g., Tarduno et al., 2015; Tang et al., 2018), in an attempt to infer crustal composition, surface environment, geodynamics and even life in the Hadean. However, any interpretation of the Hadean detrital zircon record critically depends on the ability to derive precise and accurate U-Pb ages (e.g., Whitehouse et al., 2017a).

U-Pb dating of ancient zircon grains like those from the Jack Hills is commonly complicated by radiogenic Pb (Pb*) loss (Corfu, 2013, and references therein). More rarely, apparent Pb* gain has also been involved to explain reversely discordant data revealed using various U-Pb dating techniques (e.g., Williams et al., 1984; Mattinson et al., 1996; Carson et al., 2002; McFarlane et al., 2005; Wiemer et al., 2017), although reverse discordance can also result from matrix effect during SIMS analysis of high U zircon (e.g., White and Ireland, 2012). Recent studies using high-resolution scanning ion imaging (SII) (Kusiak et al., 2013a, b; Whitehouse et al., 2014; Ge et al., 2018), atom probe tomography (APT) (Valley et al., 2014; Peterman et al., 2016a; Piazolo et al., 2016) and transmission electron microscopy (TEM) (Kusiak et al., 2015; Whitehouse et al., 2017b) have documented abundant micrometer- to nanometer-scale Pb*-enriched domains (PEDs) with elevated Pb* concentrations in Hadean to Paleozoic zircons (see Table 1 for acronyms), providing evidence for excess Pb* that is not generated by *in-situ* U decay. Such unsupported Pb* has been ascribed to mobilization and intra-grain enrichment of Pb* (see references above). However, the PEDs documented in these studies are highly variable in Pb* concentration, and their formation mechanism remains elusive, as too does their effect on *in-situ* U-Pb dating.

For example, using SII, Kusiak et al. (2013a, b) and Whitehouse et al. (2014) found numerous micrometer-scale PEDs in partially radiation-damaged zircons that had undergone ultrahigh temperature (UHT) metamorphism. These authors carried out high-resolution TEM and demonstrated that the PEDs occur as 5 – 30 nm metallic Pb (100% Pb) nanospheres formed as trapped melt inclusions due to thermal annealing of interconnected radiation damage during UHT metamorphism. They suggested that these metallic Pb nanospheres were responsible for the reversely discordant ages observed in some in *in-situ* SIMS analyses (e.g., Black et al., 1986). However, apparently concordant yet spuriously old ages can also be obtained in ancient zircon (Fig. 1). In contrast, using APT, Valley et al. (2014) demonstrated abundant ~10 – 20 nm Y-rich clusters with ≤0.8 at.% Pb* in a ~4374 Ma zircon from the Jack Hills, which they attributed to diffusion of Y and Pb* into nanoscale radiation damage during a ~3.4 Ga metamorphic event. The authors determined that these Pb*-rich nanoclusters are homogeneously distributed throughout the analyzed volume, thereby they are unlikely to compromise micrometer-scale SIMS analyses. Similarly, Peterman et al. (2016a) found a few Pb*-enriched nanoclusters by APT in a ~2.1 Ga zircon core from the Central Greek Rhodope, but these nanoclusters have much higher Pb* concentrations (2 – 5.5 at.%) and were interpreted as Pb* trapped in dislocation loops formed by annealing of radiation damage during granulite facies metamorphism at ~150 Ma. Despite the differences in Pb* concentration and formation mechanism, all studies have suggested that radiation damage plays a vital role in the formation of PEDs. In addition, many have demonstrated that crystal plastic deformation in zircon can play an important role in the migration and redistribution of incompatible elements, including Pb* (e.g., Timms et al., 2011; Reddy et al., 2016; Piazolo et al., 2016; Kovaleva et al., 2017).

Recently, Ge et al. (2018) reported 4486 – 4425 Ma concordant SHRIMP ages from a Hadean zircon (grain 14041) from the Jack Hills with low U and Th (thus a low degree of radiation damage) and no evidence for internal deformation. Scanning ion imaging demonstrated that this zircon contains abundant micrometer-scale PEDs and that the exceptionally old SHRIMP ages were spurious and resulted from incorporation of PEDs in the analyzed volume. This case study confirms that apparently concordant ages that are up to ~200 Myr older than the crystallization ages can be obtained during *in-situ* U-Pb dating due to the presence of PEDs in Hadean zircon (Fig. 1). It also necessitates a new mechanism for the formation of PEDs in addition to Pb* mobility due to radiation damage or plastic deformation. To evaluate how many Hadean zircon grains from the Jack Hills may have been influenced by PED formation, we carried out scanning ion imaging of 50 additional Hadean zircon grains from the Jack Hills and found seven new grains that contain PEDs. Here we present *in-situ* SHRIMP U-Pb and SII data for these newly found grains, as well as new ion images for an area of grain 14041 that was not covered in Ge et al. (2018), to better constrain the mechanisms of intracrystalline Pb* enrichment and its consequences for *in-situ* U-Pb dating of ancient zircon grains.

2. Samples and analytical procedures

Zircon grains were extracted using a high voltage pulsed power fragmentation system (SelFrag) from a meta-conglomerate sample from the W74 site, where detrital Hadean zircons were first reported from the Jack Hills, Western Australia (Compston and Pidgeon, 1986). A total of ~2500 grains were mounted in epoxy resin along with zircon reference standards (CZ3, BR266 and Temora 2). The mounts were polished, gold-coated, and imaged under reflected and transmitted light. Rapid ^{206}Pb (10s) and ^{207}Pb (10s) scans were performed using a SHRIMP II ion microprobe at the John de Laeter Center (JDLC) at Curtin University in order to identify the Hadean grains, and 215 (~9%) grains were found to have ^{207}Pb/^{206}Pb ages ≥ 3.9 Ga. High resolution cathodoluminescence (CL) images were then obtained for these ancient grains using a TESCAN MIRA3 Field Emission scanning electron microscope at the Microscopy and Microanalysis Facility (JDLC), Curtin University. Electron Backscatter Diffraction (EBSD) images were also acquired for selected grains using the same instrument equipped with an Oxford Instruments AZtec EBSD system. Based on the CL, and transmitted and reflected light images, 109 relatively pristine (without major cracks or inclusions) ≥3.9 Ga grains were selected for detailed *in-situ* zircon U–Th–Pb analyses using the same SHRIMP II. Detailed analytical settings can be found in de Laeter and Kennedy (1998) and Ge et al. (2018), and the analytical precision is typically ~0.5% for ^{207}Pb/^{206}Pb and ~1.5% for ^{206}Pb/^{238}U (1σ). U-Pb age data for the grains described in this study are presented in Supplementary Table S1. Most Hadean zircon grains from the Jack Hills show some complexity in their U-Pb ages, including: 1) multiple concordant yet variable ages within the same growth zone; 2) discordant and, more rarely, reversely discordant ages; and 3) higher-than-normal analytical uncertainties. This reaffirms that ancient (and recent) Pb* mobilization is common in these grains.

To better understand the behavior of the U-Pb isotopic system, SII and dating were carried out on 51 grains that showed some degree of U-Pb complexity, including additional images of grain 14041 described in Ge et al. (2018). The analyses were performed on a CAMECA IMS1280 ion microprobe at the NordSIM Facility, Swedish Museum of Natural History, Stockholm. The analytical procedure is described in Kusiak et al. (2013b, 2013a), Whitehouse et al. (2014), Bellucci et al. (2016, 2018) and Ge et al. (2018). This technique enables high-resolution (down to 2 μm) mapping of the U-Th-Pb isotopes over an area of ~70 μm × 70 μm on the sample surface (Fig. 2). Compared to earlier studies (Kusiak et al., 2013b, 2013a; Whitehouse et al., 2014), recent procedures, using a stronger primary beam (5 μm, ~250 pA, compared to 2 μm, 100 pA), also enables calculation of $^{206}Pb/^{238}U$ ages, in addition to $^{207}Pb/^{206}Pb$ ages, for regions of interest (ROIs) of any shape and size (Bellucci et al., 2016, 2018; Ge et al., 2018). The precision depends on the size of the selected ROIs. For ROIs equivalent in size to a typical SIMS U-Pb analytical spot (~20 μm), the precision is ~1.5% for $^{207}Pb/^{206}Pb$ and ~4.5% for $^{206}Pb/^{238}U$ (1σ).

3. Results

3.1. Internal structures and SHRIMP U-Pb ages

The zircon grains in this study are reddish-brown in color and are ~100 – 200 μm long. Grain 14041, described in detail in Ge et al. (2018), contains a dark-CL, homogenous core surrounded by irregular domains with variable CL intensity and complex structures (Fig. 2a). The other seven grains (Fig. 2b – h) are either fragments (grains 11085, 12070, 14121, 22025 and 25025) or prismatic crystals (grains 13015 and 23092). Most grains show fine concentric zoning (grains 11085, 13015 and 23029, and part of grain 22026) or homogenous structure (grain 12070 and part of grain 22026) in the core, which is surrounded by multiple growth rings with variable CL intensity and patchy or homogenous structure. The oscillatory-zoned parts of grains 13015 and 23092 are locally embayed by dark-CL, homogenous domains (Fig. 2d, g). Grain 14121 is dominated by a grey-CL domain that is partly replaced by bright-CL domains (Fig. 2e). It contains abundant dark-CL fibrous structures that resemble fluid channels observed in hydrothermal experiments on zircon (cf. Fig. 1e - g in Geisler et al., 2003). Grain 25025 has a dark-CL domain and a bright-CL domain, both showing faint, fine banding (Fig. 2h). Most grains contain minor cracks, except for grain 23092 that has abundant cracks, as well as muscovite and quartz inclusions (Fig. 2g).

EBSD mapping shows that most grains (14041, 11085, 12070, 13015 and 25025) have high crystallinity and show little variation in crystal orientation, indicating limited radiation damage and no significant internal plastic deformation (Supplementary Fig. S2a – d, h). However, the dark-CL, high-U domains of grains 22026 and 23092 have low crystallinity (Fig. S2f, g), suggesting significant radiation damage. Furthermore, grain 14121 shows 2 - 4° variation of crystal orientation at the margins probably due to block rotation along fractures (Fig. S2e). But taken overall, none of these grains shows significant internal deformation.

SHRIMP U-Pb ages of grain 14041 were presented in Ge et al. (2018) and selected ages are shown in Fig. 2a. This grain yielded a large range of concordant U-Pb ages from ~4.5 – 4.0 Ga, with the oldest six analyses yielding a concordia age of 4463 ± 17 Ma (2σ), the oldest apparent age from a terrestrial zircon (Ge et al., 2018). SHRIMP data for the other grains are presented in Supplementary Table S1 and are shown in Fig. 2b – h and Fig. 5. Multiple SHRIMP analyses on the cores of grains 11085, 12070 and 13015 yielded concordant and self-consistent ages, with weighted mean $^{207}Pb/^{206}Pb$ ages of 4096 ± 9 Ma (2σ, MSWD = 0.0031, n = 2), 4029 ± 7 Ma (2σ, MSWD = 2.0, n = 4) and 4119 ± 12 Ma (2σ, MSWD = 0.78, n = 2), respectively. However, analyses on the growth rings or recrystallized domains of these grains yielded different ages to the cores (Fig. 2b –

d, Table S1): the dark-CL ring of grain 11085 yielded an indistinguishable, but reversely discordant, age (4078 ± 28 Ma, 2σ, discordance (disc.) = –4%), the grey-CL ring of grain 12070 yielded a discordant and imprecise age (3980 ± 148 Ma, 2σ, disc. = +15%), whereas the recrystallized domain of grain 13015 yielded a concordant and slightly older age (4138 ± 12 Ma, 2σ, disc. = –2%). Four analyses were performed on grain 14121 and the oldest two yielded a concordia age of 4170 ± 12 Ma (2σ, MSWD of concordance and equivalence = 2.1), the other two analyses are also concordant, but are younger and imprecise (Fig. 2e, Table S1). Four analyses of grain 22026 are all concordant, with the oldest three yielding a weighted mean $^{207}Pb/^{206}Pb$ age of 4198 ± 10 Ma (2σ, MSWD = 1.18) and the other analysis being slightly younger (4152 ± 5 Ma, 1σ, Fig. 2f, Table S1). Five analyses on the core of grain 23092 only yielded one concordant age (4183 ± 10 Ma, 2σ); the others are younger and discordant (Fig. 2g, Table S1). Grain 25025 also yielded slightly discordant ages for both the dark-CL domain (4039 ± 4 Ma 1σ, disc. = +4%) and the bright-CL domain (3999 ± 26 Ma, 1σ, disc. = +10%, Fig. 2h, Table S1).

3.2. Scanning ion imaging

3.2.1 Distribution of U-Th-Pb isotopes and its correlation with zircon structures

A new ion image of grain 14041 was collected from an area (image 2 in Fig. 2a) not previously covered by image 1 (see Fig. 2a) presented in Ge et al. (2018). The results, along with ion images for the other grains, are presented in Fig. 3 and supplementary Fig. S1. The most conspicuous feature is the extremely high U and Th contents along the margins of grains 14041, 11085, 22026 and 20025 and the cracks in grains 12070 and 23092 (Fig. 3, Fig. S1); see also Bellucci et al., 2018). These high U and Th domains mostly correlated with a slight increase in ^{206}Pb, ^{207}Pb and ^{208}Pb, as well as ^{204}Pb, and ^{232}Th and ^{208}Pb are more enriched than U and uranogenic Pb, suggesting enrichment of

Th and, to a lesser extent, U in recent geological times, seemingly accompanied by addition of common Pb. It should be noted that the cracks in grain 11085 only show a slight enrichment of Th and U in a segment close to the grain margin, whereas the majority of the cracks in this grain, as well as the cracks seen in CL in grains 14041 and 13015, do not correspond to any enrichment of U-Th-Pb isotopes (cf. Bellucci et al., 2018).

Aside from the high U and Th along grain margins and cracks, the distribution of U, Th and Pb* isotopes in the ion images generally correspond well with growth zoning and CL intensity, i.e., dark-CL domains correspond to high U, Th and Pb*, and bright-CL domains correspond to low U, Th and Pb* (Fig. 3, Fig. S1; see also Bellucci et al., 2018 and Ge et al., 2018). For example, the dark-CL core in grain 14041 and the dark-CL bands in grains 12070, 22026 and 25025 are manifested by high ion intensity in the ^{238}U and $^{232}Th^{16}O$ images, although the boundaries are less sharp compared to the CL images (Fig. 3, Fig. S1). Unlike the high U-Th margins and cracks, these dark-CL, high U-Th domains correspond to a strong increase in ^{206}Pb, ^{207}Pb and ^{208}Pb, but no increase in ^{204}Pb, indicating a primary origin formed during zircon crystallization and subsequent U and Th decay in a closed system.

3.2.2 Identification of Pb enriched domains (PEDs)*

Importantly, a number of micrometer-scale hotspots with elevated ^{207}Pb and ^{206}Pb were revealed by the ion images (Fig. 3). These PEDs do not appear in the ^{238}U or ^{204}Pb images, similar to those previously described and shown in image 1 of grain 14041 by Ge et al. (2018). These PEDs occur as isolated hotspots, and the number of PEDs ($\leq$3) in each ion image is much less than that in image 1 of grain 14041 (Ge et al., 2018). Moreover, the PEDs appear to reside within different growth zones in several of the grains. For example, in grain 14041 they are mostly located at the margin of the bright-CL recrystallized domains (Fig. 3a, see also Ge et al., 2018). Two PEDs in grain 11085 are aligned parallel to a thin dark-CL growth zone at the margin of the core, whereas a third one is located in the dark-CL homogenous growth ring (Fig. 3b). Two PEDs in grain 12070 are associated with two thin dark-CL bands surrounding the core (Fig. 3c), whereas the two PEDs in grain 13015 are located in the recrystallized domain that truncates the core (Fig. 3d). One PED in grain 14121 is also located at the margin of a bright-CL domain, but the other one resides in the grey-CL domain (Fig. 3e). The single PEDs in grains 22026 and 25025 are located in dark-CL, high U bands (Fig. 3f and h, respectively), whereas the PED in grain 23092 is in a grey-CL domain surrounded by multiple cracks (Fig. 3g).

To further characterize the PEDs, isotope profiles recording the ^{238}U, ^{207}Pb and ^{206}Pb counts, as well as the ^{207}Pb/^{206}Pb ratios, were extracted from a transect of small squares (~2 μm × 2 μm) along a profile that bisects the PEDs (Fig. 4). The results show that the PEDs correspond to ^{207}Pb and ^{206}Pb peaks, but that the ^{238}U counts remain constant. They also correspond to striking peaks in ^{207}Pb/^{206}Pb ratios (up to 0.7 – 1.1 in different grains), resulting in apparent ^{207}Pb/^{206}Pb ages from 4.7 to 5.4 Ga (Fig. 4). This is in contrast with the dark-CL core of grain 14041 and the dark-CL zones in grains 22026 and 25025, where the elevated ^{207}Pb and ^{206}Pb counts are supported by elevated ^{238}U and the ^{207}Pb/^{206}Pb ratios remain constant (Fig. 4). These observations confirm that the PEDs represent local concentration of unsupported ancient Pb*. The cracks in grain 23092 are characterized by elevated peaks in ^{238}U, but no peaks in ^{207}Pb or ^{206}Pb (Fig. 4g), consistent with recent influx of U (and Th).

3.2.3 U-Pb ages calculated from ion images

To test the effect of the PEDs on *in-situ* ion microprobe U-Pb dating, and to better constrain the ages of the grains, U-Pb ages were calculated from the ion images for three sets of ROIs: 1) ~5 μm ellipse similar in size to the PEDs in the ion images; 2) ~20 μm ellipse similar to *in-situ* SIMS U-Pb analytical spots; and 3) polygons that broadly correspond to growth zones seen in the CL images. The results are presented in Supplementary Table S2 and are shown in Figs. 3 and 5. Generally, the ~5 μm ellipse located on the PEDs yielded exceptionally old ages, mostly exceeding the age of the Earth (Figs. 3 and 5, Table S2). These data are mostly reversely discordant (^{207}Pb/^{206}Pb age $<$ ^{206}Pb/^{238}U age), but intercept concordia due to large uncertainties in the ^{206}Pb/^{238}U ages, which are largely propagated from the U/Pb calibration. The ~20 μm ellipses incorporating PEDs mostly yielded significantly older ages than the SHRIMP analyses in the same domain and the assigned crystallization age of each grain. In contrast, ~20 μm ellipses that do not include the PEDs generally yielded ages consistent with the SHRIMP data. These results confirm that incorporation of PEDs during *in-situ* SIMS analyses results in spuriously old ages that may be hundreds of million years older than the crystallization ages (Ge et al., 2018).

The calculated ages for the polygons following growth zones provide interesting insights into the formation of the PEDs. Most polygons, with or without PEDs, yield concordant ages that are, within uncertainties, indistinguishable from the SHRIMP ages (last panel in Fig. 3, Table S2), suggesting that the PEDs mostly formed within individual growth zones and that their effect on the calculated age was diminished because of the small size of the area they occupied. However, the polygon that includes the PEDs in Image 2 of grain 14041 (ROI 10) has a discordant age (^{207}Pb/^{206}Pb age of ~4.16 Ga), which is younger that the ~4.3 Ga crystallization age of this grain (Ge et al., 2018). This is also true for the dark-CL zone (ROI 3) containing the PED in grain 22026. The polygons including the PEDs in grain 14121 (ROIs 7 and 9) yield concordant ages (~4.12 Ga) that are also slightly younger than the crystallization age of this grain (~4.17 Ga) based on SHRIMP analyses. These observations suggest that these regions might have experienced an overall Pb* loss despite the presence of PEDs.

The U-Pb ages calculated for the polygons also provide further constraints on the crystallization ages of the studied grains. For example, SHRIMP analyses of grain 23092 predominantly yielded discordant ages, due to high U and Th along ubiquitous cracks. Small polygons were carefully selected in the ion images to avoid these cracks, yielding concordant ages with a weighted mean $^{207}Pb/^{206}Pb$ age of 4177 ± 29 Ma (2σ, MSWD = 1.8, n = 7, Table S2, Fig. 5g), consistent with the oldest concordant SHRIMP analysis (4185 ± 10 Ma, 2σ, Table S1, Fig. 2g). In addition, polygons overlapping individual secondary growth rings or recrystallized domains mostly yielded ages indistinguishable from, or slightly younger than, the crystallization ages of individual grains (Fig. 5), suggesting these grains were overprinted shortly after crystallization in the Hadean.

4. Discussion

4.1. Characteristics of the PEDs in Hadean zircons from the Jack Hills

The ion images show the distribution of U, Th and Pb isotopes within zircon and confirm their correlation with internal growth zones as seen in CL images, except for the extremely high U and Th along grain margins and some of the cracks, which probably resulted from growth of secondary xenotime during low-grade metamorphism (e.g., Rasmussen et al., 2011; Bell et al., 2015b) and/or interaction with weathering solutions in recent geological times (Pidgeon et al., 2017, and references therein). They also provide solid evidence for the presence of micrometer-scale hotspots of unsupported Pb* (i.e., PEDs) in the Hadean zircon grains. The isotope profiles and calculated U-Pb ages presented above demonstrate that the PEDs represent ancient Pb* that has been locally concentrated within zircon. They have at least 2 – 5 times higher Pb* concentrations than the surrounding regions and are not accompanied by elevated U, Th or ^{204}Pb, indicating that the Pb* is neither produced by *in-situ* U or Th decay, nor the result of introduction of common Pb. Moreover, the PEDs have extremely high ^{207}Pb/^{206}Pb ratios (up to 0.7 – 1.1) that correspond to apparent ages well in excess of the age of the Earth, suggesting that the Pb* was produced within a few hundred million years after the crystallization of the Hadean zircons when radiogenic ^{207}Pb was relatively more abundant because of the higher abundance and faster decay of ^{235}U. It should be noted that these estimates of Pb concentrations and ^{207}Pb/^{206}Pb ratios are minimum values, because the actual size of the PEDs is likely to be much less than a few microns (see below), so that even the smallest ROIs selected for calculation represent a mixture of Pb* in the PEDs and Pb* produced by subsequent *in-situ* decay.

Previously, PEDs have been documented using SII in Archean zircons from the Napier Complex, East Antarctica (Kusiak et al., 2013a, b), and in Paleoproterozoic zircons from the Kerala Khondalite Belt, southern India (Whitehouse et al., 2014), both of which were from rocks that have undergone UHT metamorphism. However, the PEDs are much rarer in the detrital Hadean zircons from the Jack Hills than in those two earlier studies. Only 1 – 3 hotspots are found in the ~70 μm × 70 μm imaged areas in most grains, compared to tens to hundreds in the Antarctic and Indian zircon grains (Kusiak et al., 2013a, b; Whitehouse et al., 2014). Relatively abundant PEDs are only present in a small area (image 1) of grain 14041 (Ge et al., 2018). This suggests that Pb* mobilization and redistribution in the Jack Hills Hadean zircon grains mostly occurred within specific zones (see below), consistent with the fact that most grains yielded precise U-Pb ages.

Recent APT (Valley et al., 2014; Peterman et al., 2016a; Piazolo et al., 2016) and TEM

(Kusiak et al., 2015; Whitehouse et al., 2017b) studies reveal that PEDs in zircon commonly occur as 5 – 30 nm clusters or patches, which is about three orders of magnitude less than the size of the Pb* hotspots appearing in the ion images. This likely results from the relatively low resolution of the current ion imaging technique, which uses a ~5 μm primary beam. Whitehouse et al. (2014) carried out depth-profile ion imaging that integrated more than 1500 scans rastered over the imaged area. The crater depth of the rastered area was calibrated using a profilometer, yielding an average sputtering rate of ~0.05 nm/scan that enables resolution of 1 – 2 nm objects over the sputtering depth. The results suggest that the PEDs in the Paleoproterozoic zircon grains from the Kerala Khondalite Belt in southern India range in size from <5 nm to several 10s nm, consistent with TEM observations (Whitehouse et al., 2017b). We prepared a pseudo-3D reconstruction of the PED in grain 25025 by integrating the ^{207}Pb counts for each 10 scans and found that the intensity of the PED gradually increased and then decreased, before disappearing after 60 scans, suggesting the PED was completely traversed during sputtering and its actual size was smaller than the sputtering depth (Fig. 6). Although the current analysis used a stronger (~250 pA, ~5 μm diameter) primary beam and thus likely a higher sputtering rate than that in Whitehouse et al. (2014) (~100 pA, ~2 μm diameter), this experiment suggests that the PEDs in the Hadean zircons from the Jack Hills are probably also nano-scale objects.

4.2. Mechanisms of intra-grain Pb enrichment*

The presence of PEDs in zircon indicates that Pb* was locally concentrated within the crystal, while the whole grain or the hosting growth zone might have experienced an overall Pb* loss or remained a closed system. Thus, any mechanism for the formation of PEDs has to explain not only Pb* mobilization at various scales but also capture of the mobilized Pb* at favorable nano-scale sites. As mentioned earlier, several mechanisms have been proposed for the formation of PEDs, including: 1) diffusion of Pb* into loose nanoclusters, produced initially by α-recoil damage, but enhanced during later reheating (Valley et al., 2014); 2) trace element (including Pb*) migration into fast diffusion pathways (e.g., dislocations, low-angle boundaries) produced by crystal-plastic deformation (e.g., Timms et al., 2011; Reddy et al., 2016; Piazolo et al., 2016; Kovaleva et al., 2017); 3) formation of metallic Pb nanospheres in partially radiation-damaged zircon during later UHT metamorphism (Kusiak et al., 2015; Whitehouse et al., 2017b); and 4) Pb* trapped in dislocation loops during high temperature metamorphism (Peterman et al., 2016a). Mechanisms 1), 3), and 4) are all related to radiation damage, but are different in the resultant Pb* concentrations in the PEDs, and thus have different geochronological implications.

The PEDs formed by mechanism 1) have relatively low Pb* concentrations (≤0.8 at.%) and are homogenously distributed within the micrometer-scale spot-size of SIMS analyses (Valley et al., 2014). This is probably because Pb diffusion in zircon is relatively slow even under very high temperatures (e.g., Cherniak and Watson, 2001) and thus is unable to mobilize and concentrate Pb to a greater extent. This mechanism is inconsistent with the heterogeneous distribution of the PEDs in this study, which have much higher Pb* concentrations and have compromised some of the SHRIMP spot analyses (Ge et al., 2018). Mechanism 2, i.e., deformation-induced trace element mobilization, can also be ruled out here, since EBSD mapping of the grains shows little internal deformation, except for minor (<2 – 4°) misorientations at the margins for some grains, which are unrelated to any PEDs (Figs. 3 and 4).

The metallic Pb nanosphere model, mechanism 3) (Kusiak et al., 2015; Whitehouse et al., 2017b), and the dislocation loop model, mechanism 4) (Peterman et al., 2016a), both involve thermal annealing of interconnected radiation damage during a high-temperature event. The resultant PEDs have variably high Pb* concentrations (100% Pb* for metallic Pb nanospheres and 2 – 5.5 at. % for dislocation loops) and are heterogeneously distributed, and thus are easily detected during SIMS analysis. The degree of radiation damage depends on the U and Th contents and the time between crystallization and annealing (e.g., Murakami et al., 1991). We have estimated the time of the overprinting event that led to Pb* mobilization for each grain using the lower intercept age of the discordia that is anchored at the crystallization age and fitted to the SHRIMP and ion imaging data, excluding outliers (Fig. 5). The resultant lower intercept ages range from 4.1 to 3.3 Ga (Fig. 5, Table 2), except for ~2.8 Ga for grain 13015, which is probably too young because the SHRIMP and ion image ages for the domain that contains PEDs are concordant and consistent with the crystallization age, indicating Pb* mobilization shortly after crystallization at ~4.1 Ga. These estimated Pb mobilization ages are older than the ~3.0 Ga maximum deposition age of the conglomerate that contains the Hadean zircon grains (e.g., Compston and Pidgeon, 1986), suggesting Pb* mobilization occurred in the source rock(s) at earlier, but different times (Table 2), rather than during a post-deposition overprinting event that influence the entire zircon population. Indeed, the timing of the oldest metamorphism at the W74 site was determined at 2653±5 Ma utilizing metamorphic monazite (Rasmussen et al., 2010), and is considerably younger than any of the lower intercept ages. Accordingly, the α-dose was calculated using the U and Th contents of the domains containing the PEDs. The resultant α-dose at the time of Pb* mobilization is $0.1 – 1.2 \times 10^{15}$/mg (Table 2), which is below the first percolation point (~2.2×10^{15}/mg) (Pidgeon, 2014), suggesting these grains were not significantly damaged when Pb* mobilization occurred. However, the PEDs in grains 11085, 12070, 22026 and 25025 are exclusively associated with dark-CL, high

U growth zones, which could have accumulated considerably more radiation damage than adjacent zones. A recent TEM study (Tang et al., 2018) revealed abundant nanoscale pores and interconnected dislocations in relatively high U growth zones in Jack Hills zircons, which are partly filled with Fe-oxides, but could also have been favorable sites for Pb* concentration. Therefore, we suggest that Pb* trapped at these sites during thermal annealing of local-scale radiation damaged areas in these zones was likely responsible for producing the PEDs.

However, the radiation damage annealing model cannot explain the PEDs in grains 14041, 13015 and 14121, which are located in, or near the margin of, relatively bright-CL, low-U domains, whereas the relatively dark-CL, high-U domains (e.g., the CL-dark core of grain 14041 and the regularly zoned core of grain 13015) in the same grains are PED-free (Fig. 3; also see Ge et al., 2018). These bright-CL domains have irregular or curved boundaries and patchy or homogenous internal structures that truncate or embay the regularly zoned or homogeneous, high-U domains. They are also characterized by low Th contents and low Th/U ratios relative to the regularly zoned or homogenous domains (e.g., average Th = 3 ppm and Th/U = 0.11 for grain 14041, Ge et al., 2018). These characteristics are consistent with preferential expulsion of Th over U during solid-stage recrystallization in the presence of an aqueous fluid (e.g., Pidgeon, 1992; Vavra et al., 1996; Schaltegger et al., 1999; Corfu et al., 2003), suggesting that the PEDs in these grains are probably related to fluid-present recrystallization of non-metamict zircon.

Geisler et al. (2007) proposed a coupled dissolution-reprecipitation model for the recrystallization of zircon without significant radiation damage. This model involves dissolution of trace element-rich zircon and simultaneous precipitation of trace element-free zircon and trace element-rich inclusions. This process has been documented in many natural zircons that show clear evidence of fluid alteration, but did not accumulate significant radiation damage at the time of alteration (e.g., Tomaschek et al., 2003; Rubatto et al., 2008; Kusiak et al., 2009; Soman et al., 2010; Peterman et al., 2016b; Chen and Zhou, 2017; Vonlanthen et al., 2012). The resultant recrystallized domain is characterized by relatively bright CL intensity, low trace element concentrations and low Th/U ratios, as well as the presence of pores and mineral inclusions ranging from nanometers to micrometers in size (see references above). Putnis (2002) argued that coupled dissolution-reprecipitation is a very common replacement reaction occurring in many minerals or mineral assemblages in disequilibrium with a fluid, and that the development of porosity is a general consequence of loss of some reactant materials to the fluid (see also Geisler et al., 2007). In altered zircons ascribed to this process, micrometer-scale pores and mineral inclusions have been observed using SEM (e.g., Tomaschek et al., 2003; Rubatto et al., 2008; Kusiak et al., 2009; Soman et al., 2010; Peterman et al., 2016b; Chen and Zhou, 2017), and nanometer-scale pores, strain centers and dislocation loops have been documented using high-resolution TEM (Vonlanthen et al., 2012; Tang et al., 2018). Vonlanthen et al. (2012) further suggested that these pores could have been remnants of transport channels of incompatible trace elements, including Pb*, which, upon annealing, could have been trapped in the zircon lattice. Kusiak et al. (2009) found that the recrystallized zircon domains in altered Paleozoic zircons from the Bohemian Massif yielded strongly reversely discordant U-Pb ages, in part due to a matrix effect during SIMS analysis but in part also to presence of unsupported Pb*.

Accordingly, we suggest that Pb* trapped in nanoscale pores formed during fluid infiltration and recrystallization could have been responsible for the PEDs associated with the relatively bright-CL domains in zircon grains 14041, 13015 and 14121 from the Jack Hills. This interpretation is supported by the fibrous structures seen in grain 14121 (Fig. 2e), which are very similar to fluid channels produced in altered zircon rims during hydrothermal experiments (see Fig. 1e - g in Geisler et al., 2003). However, the absence of identifiable mineral inclusions in these grains is inconsistent with this model, although a fluid inclusion can be seen deeply buried in grain 14041 based on transmitted light photomicrographs (Fig. S3). It is likely that most trace element-rich mineral inclusions are incompatible in the zircon lattice and may have been expulsed during recrystallization.

4.3 Implications for in-situ U-Pb dating

The presence of PEDs in zircon constitutes a challenge for low-volume U-Pb dating (e.g., *in-situ* SIMS analysis), especially for ancient detrital zircon grains like those from the Jack Hills. Our results demonstrate that a significant portion (at least ~14%) of detrital Hadean zircon grains from the Jack Hills contain PEDs, which have high Pb* concentrations and high $^{207}Pb/^{206}Pb$ ratios so that including even small portions in a SIMS spot would produce spuriously old $^{207}Pb/^{206}Pb$ and $^{206}Pb/^{238}U$ ages. Whether the resultant ages are reversely discordant or concordant depends on the time of PED formation and the analytical precision, which is likely compromised by the heterogeneous distribution of PEDs in the analyzed volume. Apparently concordant ages can be obtained if the PEDs formed within a few hundred million years after crystallization, even for the typical precision of SIMS analyses (see Fig. 1; Ge et al., 2018). Overprinting by later Pb* loss events would also transfer the reversely discordant data onto the concordia curve. The implication is that concordance is no longer a guarantee of the reliability of U-Pb ages, even if multiple concordant ages, or a concordia age, have been obtained. This has been substantiated by the spuriously old concordia age of grain 14041 (Ge et al., 2018), although, in general, the possibility to encounter PEDs during *in-situ* SIMS dating of the Jack Hills Hadean zircon grains is low considering the rarity of PEDs in most of the studied grains. To overcome this possibility, the intra-grain distribution of U-Th-Pb isotopes should be carefully investigated for grains showing complex age spectra, and regions showing evidence of disturbance of the U-Th-Pb isotopic system, e.g., PEDs, high U-Th margins and cracks, should be avoided in order to extract primary crystallization ages.

This study also highlights that Pb* behavior in zircon may be more complicated than previously thought. Pb* can be mobilized and migrated out (Pb* loss), or be concentrated (PED formation), in various regions of a zircon through diverse mechanisms. This can occur not only during crystal plastic deformation or high- to ultra-high temperature metamorphism in partially metamict zircon, but also under relatively low temperature, fluid-present conditions in undamaged zircon as early as ~4.1 Ga. Better understanding of these processes, probably by a combination of high-resolution techniques (e.g., SII, APT and TEM), is essential for proper interpretation of complex U-Pb age spectra in zircon.

Conclusions

Scanning ion imaging reveals that 8 out of 51 Hadean detrital zircon grains from the Jack Hills contain micrometer-scale PEDs, indicating that these ancient zircon grains were affected by intra-crystalline Pb* enrichment. The PEDs are relatively rare in most of the grains and reside in different growth zones, suggesting they may have formed on a local-scale. The PEDs associated with dark-CL, high-U zones are interpreted as Pb* trapped during thermal annealing of local-scale inter-connected radiation damaged areas, whereas those associated with bright-CL recrystallized domains resulted from Pb* concentration in nanoscale pores formed during fluid-present recrystallization of non-metamict zircon. Our interpretations imply that PEDs formed at favorable local sites, with the majority of the grain not affected by Pb* mobilization. This also implies that the formation mechanism of PEDs in zircon is more diverse than previously thought. These PEDs in the Hadean zircon grains have high Pb* concentrations and high $^{207}Pb/^{206}Pb$ ratios such that incorporating them into micrometer-scale SIMS spots will produce spuriously old ages. The resultant U-Pb data are either reversely discordant or concordant, depending on the time of Pb* mobilization and the analytical precision. The presence of PEDs explains reversely discordant, imprecise and/or exceptionally old SIMS ages recorded in some ancient zircons and implies that intra-grain distribution of U-Th-Pb isotopes needs to be carefully evaluated in order to obtain reliable crystallization ages in such zircons.

Acknowledgements

We thank Adam Frew and Eric Thern for assistance with SHRIMP analysis, and Elaine Miller, Zakaria Quadir, and Kelly Merigot for assistance with CL, BSE, and EBSD imaging. We also thank F. Corfu, E. Bell and F. Moynier (editor) for constructive reviews and suggestions. This study is supported by the Australia Research Council Centre of Excellence for Core to Crust Fluid Systems (CCFS, contribution 1333), the Knut and Alice Wallenberg Foundation and the Swedish Research Council to Whitehouse and Nemchin, and the National Natural Science Foundation of China (41672186 and 41502178) to R. Ge. NordSIM is a joint Swedish-Icelandic analytical facility, of which this is contribution 597.

References

Amelin, Y., Lee, D.C., Halliday, A.N., Pidgeon, R.T., 1999. Nature of the Earth's earliest crust from hafnium isotopes in single detrital zircons. Nature 399, 252-255.

https://doi.org/doi:10.1038/20426.

Bell, E.A., Boehnke, P., Harrison, T.M., Mao, W.L., 2015a. Potentially biogenic carbon preserved in a 4.1 billion-year-old zircon. Proc. Nat. Ac. Sci. 112, 14518-14521. https://doi.org/10.1073/pnas.1517557112.

Bell, E.A., Boehnke, P., Hopkins-Wielicki, M.D., Harrison, T.M., 2015b. Distinguishing primary and secondary inclusion assemblages in Jack Hills zircons. Lithos 234, 15-26. https://doi.org/10.1016/j.lithos.2015.07.014.

Bellucci, J.J., Nemchin, A.A., Whitehouse, M.J., Kielman, R.B., Snape, J.F., Pidgeon, R.T., 2018. Geochronology of Hadean zircon grains from the Jack Hills, Western Australia constrained by quantitative scanning ion imaging. Chem. Geol. 476, 469-480. https://doi.org/10.1016/j.chemgeo.2017.11.042.

Bellucci, J.J., Whitehouse, M.J., Nemchin, A.A., Snape, J.F., Pidgeon, R.T., Grange, M., Reddy, S.M., Timms, N., 2016. A scanning ion imaging investigation into the micron-scale U-Pb systematics in a complex lunar zircon. Chem. Geol. 438, 112-122. https://doi.org/10.1016/j.chemgeo.2016.05.022.

Black, L.P., Williams, I.S., Compston, W., 1986. Four zircon ages from one rock: the history of a 3930 Ma-old granulite from Mount Sones, Enderby Land, Antarctica. Contrib. Mineral. Petr. 94, 427-437.

Carson, C.J., Ague, J.J., Grove, M., Coath, C.D., Harrison, T.M., 2002. U–Pb isotopic behaviour of zircon during upper-amphibolite facies fluid infiltration in the Napier Complex, east Antarctica. Earth. Planet. Sci. Lett. 199, 287-310.

Chen, W.T., Zhou, M., 2017. Hydrothermal alteration of magmatic zircon related to NaCl-rich brines: Diffusion-reaction and dissolution-reprecipitation processes. Am. J. Sci. 317, 177-215.

Cherniak, D.J., Watson, E.B., 2001. Pb Diffusion in Zircon. Chem. Geol. 172, 5-24.

Compston, W.T., Pidgeon, R.T., 1986. Jack Hills, evidence of more very old detrital zircons in Western Australia. Nature 321, 766-769.

Corfu, F., 2013. A century of U-Pb geochronology: The long quest towards concordance. Geol. Soc. Am. Bull. 125, 33 -47. https://doi.org/10.1130/B30698.1.

Corfu, F., Hanchar, J.M., Hoskin, P.W.O., Kinny, P., 2003. Atlas of Zircon Textures. Reviews in Mineralogy and Geochemistry 53, 469 -500. https://doi.org/10.2113/0530469.

de Laeter, J.R., Kennedy, A.K., 1998. A double focusing mass spectrometer for geochronology. Int. J. Mass Spectrom. 178, 43-50. https://doi.org/10.1016/S1387-3806(98)14092-7.

Ge, R., Wilde, S.A., Nemchin, A.A., Whitehouse, M.J., Bellucci, J.J., Erickson, T.M., Frew, A., Thern, E.R., 2018. A 4463 Ma apparent zircon age from the Jack Hills (Western Australia) resulting from ancient Pb mobilization. Geology 46, 303-306. https://doi.org/10.1130/G39894.1.

Geisler, T., Pidgeon, R.T., Kurtz, R., Van Bronswijk, W., Schleicher, H., 2003. Experimental hydrothermal alteration of partially metamict zircon. Am. Mineral. 88, 1496 -1513.

Geisler, T., Schaltegger, U., Tomaschek, F., 2007. Re-equilibration of zircon in aqueous fluids and melts. Elements 3, 43-50. https://doi.org/10.2113/gselements.3.1.43.

Holden, P., Lanc, P., Ireland, T.R., Harrison, T.M., Foster, J.J., Bruce, Z., 2009. Mass-spectrometric mining of Hadean zircons by automated SHRIMP multi-collector and single-collector U/Pb zircon age dating: the first 100,000 grains. Int. J. Mass Spectrom. 286, 53-63. https://doi.org/10.1016/j.ijms.2009.06.007.

Hopkins, M., Harrison, T.M., Manning, C.E., 2008. Low heat flow inferred from> 4 Gyr zircons suggests Hadean plate boundary interactions. Nature 456, 493-496. https://doi.org/10.1038/nature07465.

Kemp, A.I.S., Wilde, S.A., Hawkesworth, C.J., Coath, C.D., Nemchin, A., Pidgeon, R.T., Vervoort, J.D., Dufrane, S.A., 2010. Hadean crustal evolution revisited: New constraints from Pb-Hf isotope systematics of the Jack Hills zircons. Earth. Planet. Sci. Lett. 296, 45-56. https://doi.org/doi: 10.1016/j.epsl.2010.04.043.

Kovaleva, E., Klötzli, U., Habler, G., Huet, B., Guan, Y., Rhede, D., 2017. The effect of crystal-plastic deformation on isotope and trace element distribution in zircon: Combined BSE, CL, EBSD, FEG-EMPA and NanoSIMS study. Chem. Geol. 450, 183-198. https://doi.org/10.1016/j.chemgeo.2016.12.030.

Kusiak, M.A., Dunkley, D.J., Słaby, E., Martin, H., Budzyń, B., 2009. Sensitive high-resolution ion microprobe analysis of zircon reequilibrated by late magmatic fluids in a hybridized pluton. Geology 37, 1063-1066.

Kusiak, M.A., Dunkley, D.J., Wirth, R., Whitehouse, M.J., Wilde, S.A., Marquardt, K., 2015. Metallic lead nanospheres discovered in ancient zircons. Proc. Nat. Ac. Sci. 112, 4958-4963. https://doi.org/10.1073/pnas.1415264112.

Kusiak, M.A., Whitehouse, M.J., Wilde, S.A., Dunkley, D.J., Menneken, M., Nemchin, A.A., Clark, C., 2013b. Changes in zircon chemistry during Archean UHT metamorphism in the Napier Complex, Antarctica. Am. J. Sci. 313, 933 -967. https://doi.org/doi: 10.2475/09.2013.05.

Kusiak, M.A., Whitehouse, M.J., Wilde, S.A., Nemchin, A.A., Clark, C., 2013a. Mobilization of radiogenic Pb in zircon revealed by ion imaging: Implications for early Earth geochronology.

Geology 41, 291 -294. https://doi.org/doi: 10.1130/G33920.1.

Maas, R., Kinny, P.D., Williams, I.S., Froude, D.O., Compston, W., 1992. The Earths oldest known crust - A geochronological and geochemical study of 3900-4200 Ma old detrital zircons from Mt Narryer and Jack Hills, Western-Australia. Geochim. Cosmochim. Acta 56, 1281-1300. https://doi.org/10.1016/0016-7037(92)90062-N.

Mattinson, J.M., Graubard, C.M., Parkinson, D.L., McClelland, W.C., 1996. U‐Pb reverse discordance in zircons: The role of fine‐scale oscillatory zoning and sub‐micron transport of Pb. In: Basu, A., Hart, S. (Eds.), Earth processes: reading the isotopic code. In: Geophysical Monograph, Washington DC, American Geophysical Union, pp. 355-370.

McFarlane, C.R.M., Connelly, J.N., Carlson, W.D., 2005. Intracrystalline redistribution of Pb in zircon during high-temperature contact metamorphism. Chem. Geol. 217, 1-28. https://doi.org/10.1016/j.chemgeo.2004.11.019.

Murakami, T., Chakoumakos, B.C., Ewing, R.C., Lumpkin, G.R., Weber, W.J., 1991. Alpha-decay event damage in zircon. Am. Mineral. 76, 1510-1532.

Nemchin, A.A., Pidgeon, R.T., Whitehouse, M.J., 2006. Re-evaluation of the origin and evolution of >4.2 Ga zircons from the Jack Hills metasedimentary rocks. Earth. Planet. Sci. Lett. 244, 218-233. https://doi.org/10.1016/j.epsl.2006.01.054.

Peterman, E.M., Reddy, S.M., Saxey, D.W., Snoeyenbos, D.R., Rickard, W.D., Fougerouse, D., Kylander-Clark, A.R., 2016a. Nanogeochronology of discordant zircon measured by atom probe microscopy of Pb-enriched dislocation loops. Sci. Adv. 2, e1601318. https://doi.org/10.1126/sciadv.1601318.

Peterman, E.M., Snoeyenbos, D.R., Jercinovic, M.J., Kylander-Clark, A., 2016b. Dissolution-reprecipitation metasomatism and growth of zircon within phosphatic garnet in metapelites from western Massachusetts. Am. Mineral. 101, 1792-1806.

Piazolo, S., La Fontaine, A., Trimby, P., Harley, S., Yang, L., Armstrong, R., Cairney, J.M., 2016. Deformation-induced trace element redistribution in zircon revealed using atom probe tomography. Nat. Commun. 7. https://doi.org/10.1038/ncomms10490.

Pidgeon, R.T., 1992. Recrystallization of Oscillatory Zoned Zircon - Some Geochronological and Petrological Implications. Contrib. Mineral. Petr. 110, 463-472.

Pidgeon, R.T., 2014. Zircon radiation damage ages. Chem. Geol. 367, 13-22. https://doi.org/10.1016/j.chemgeo.2013.12.010.

Pidgeon, R.T., Nemchin, A.A., Whitehouse, M.J., 2017. The effect of weathering on U–Th–Pb and oxygen isotope systems of ancient zircons from the Jack Hills, Western Australia. Geochim. Cosmochim. Acta 197, 142-166. https://doi.org/10.1016/j.gca.2016.10.005.

Putnis, A., 2002. Mineral replacement reactions: from macroscopic observations to microscopic mechanisms. Mineral. Mag. 66, 689-708.

Rasmussen, B., Fletcher, I.R., Muhling, J.R., Greclory, C.J., Wilde, S.A., 2011. Metamorphic replacement of mineral inclusions in detrital zircon from Jack Hills, Australia: Implications for the Hadean Earth. Geology 39, 1143. https://doi.org/10.1130/G32554.1.

Rasmussen, B., Fletcher, I.R., Muhling, J.R., Wilde, S.A., 2010. In situ U–Th–Pb geochronology of monazite and xenotime from the Jack Hills belt: Implications for the age of deposition and metamorphism of Hadean zircons. Precambrian Res. 180, 26-46. https://doi.org/https://doi.org/10.1016/j.precamres.2010.03.004.

Reddy, S.M., van Riessen, A., Saxey, D.W., Johnson, T.E., Rickard, W.D., Fougerouse, D., Fischer, S., Prosa, T.J., Rice, K.P., Reinhard, D.A., 2016. Mechanisms of deformation-induced trace element migration in zircon resolved by atom probe and correlative microscopy. Geochim. Cosmochim. Acta 195, 158-170. https://doi.org/10.1016/j.gca.2016.09.019.

Rubatto, D., Mu¨ntener, O., Barnhoorn, A., Gregory, C., 2008. Dissolution-reprecipitation of zircon at low-temperature, high-pressure conditions (Lanzo Massif, Italy). Am. Mineral. 93, 1519-1529.

Schaltegger, U., Fanning, C.M., Günther, D., Maurin, J.C., Schulmann, K., Gebauer, D., 1999. Growth, annealing and recrystallization of zircon and preservation of monazite in high-grade metamorphism: conventional and in-situ U-Pb isotope, cathodoluminescence and microchemical evidence. Contrib. Mineral. Petr. 134, 186-201. https://doi.org/10.1007/s004100050478.

Soman, A., Geisler, T., Tomaschek, F., Grange, M., Berndt, J., 2010. Alteration of crystalline zircon solid solutions: a case study on zircon from an alkaline pegmatite from Zomba–Malosa, Malawi. Contrib. Mineral. Petr. 160, 909-930. https://doi.org/10.1007/s00410-010-0514-2.

Tang, F., Taylor, R.J.M., Einsle, J.F., Borlina, C.S., Fu, R.R., Weiss, B.P., Williams, H.M., Williams, W., Nagy, L., Midgley, P.A., Lima, E.A., Bell, E.A., Harrison, T.M., Alexander, E.W., Harrison, R.J., 2018. Secondary magnetite in ancient zircon precludes analysis of a Hadean geodynamo. Proc. Nat. Ac. Sci., 201811074. https://doi.org/10.1073/pnas.1811074116.

Tarduno, J.A., Cottrell, R.D., Davis, W.J., Nimmo, F., Bono, R.K., 2015. A Hadean to Paleoarchean geodynamo recorded by single zircon crystals. Science 349, 521-524. https://doi.org/10.1126/science.aaa9114.

Timms, N.E., Kinny, P.D., Reddy, S.M., Evans, K., Clark, C., Healy, D., 2011. Relationship among titanium, rare earth elements, U–Pb ages and deformation microstructures in zircon: Implications for Ti-in-zircon thermometry. Chem. Geol. 280, 33-46. https://doi.org/10.1016/j.chemgeo.2010.10.005.

Tomaschek, F., Kennedy, A.K., Villa, I.M., Lagos, M., Ballhaus, C., 2003. Zircons from Syros, Cyclades, Greece—recrystallization and mobilization of zircon during high-pressure metamorphism. J. Petrol. 44, 1977-2002.

Trail, D., Watson, E.B., Tailby, N.D., 2011. The oxidation state of Hadean magmas and implications for early Earth/'s atmosphere. Nature 480, 79-82.

Valley, J.W., Cavosie, A.J., Ushikubo, T., Reinhard, D.A., Lawrence, D.F., Larson, D.J., Clifton, P.H., Kelly, T.F., Wilde, S.A., Moser, D.E., Spicuzza, M.J., 2014. Hadean age for a post-magma-ocean zircon confirmed by atom-probe tomography. Nat. Geosci. 3, 219-223. https://doi.org/10.1038/ngeo2075.

Valley, J.W., Peck, W.H., King, E.M., Wilde, S.A., 2002. A Cool Early Earth. Geology 30, 351-354. https://doi.org/10.1130/0091-7613(2002)030<0351:ACEE>2.0.CO;2.

Vavra, G., Gebauer, D., Schmid, R., Compston, W., 1996. Multiple zircon growth and recrystallization during polyphase Late Carboniferous to Triassic metamorphism in granulites of the Ivrea Zone (Southern Alps): an ion microprobe (SHRIMP) study. Contrib. Mineral. Petr. 122, 337-358. https://doi.org/10.1007/s004100050132.

Vonlanthen, P., Fitz Gerald, J.D., Rubatto, D., Hermann, J., 2012. Recrystallization rims in zircon (Valle d’Arbedo, Switzerland): An integrated cathodoluminescence, LA-ICP-MS, SHRIMP, and TEM study. Am. Mineral. 97, 369-377. https://doi.org/10.2138/am.2012.3854.

Watson, E.B., Harrison, T.M., 2005. Zircon thermometer reveals minimum melting conditions on earliest Earth. Science 308, 841-844. https://doi.org/10.1126/science.1110873.

White, L.T., Ireland, T.R., 2012. High-uranium matrix effect in zircon and its implications for SHRIMP U－Pb age determinations. Chem. Geol. 306-307, 78-91. https://doi.org/https://doi.org/10.1016/j.chemgeo.2012.02.025.

Whitehouse, M.J., Kusiak, M.A., Wirth, R., Ravindra Kumar, G.R., 2017b. Metallic Pb nanospheres in ultra-high temperature metamorphosed zircon from southern India. Miner. Petrol. 111, 467-474. https://doi.org/10.1007/s00710-017-0523-1.

Whitehouse, M.J., Nemchin, A.A., Pidgeon, R.T., 2017a. What can Hadean detrital zircon really tell us? A critical evaluation of their geochronology with implications for the interpretation of oxygen and hafnium isotopes. Gondwana Res. 51, 78-91. https://doi.org/10.1016/j.gr.2017.07.007.

Whitehouse, M.J., Ravindra Kumar, G.R., Rimša, A., 2014. Behaviour of radiogenic Pb in zircon during ultrahigh-temperature metamorphism: an ion imaging and ion tomography case study from the Kerala Khondalite Belt, southern India. Contrib. Mineral. Petr. 168, 1042. https://doi.org/10.1007/s00410-014-1042-2.

Wiemer, D., Allen, C.M., Murphy, D.T., Kinaev, I., 2017. Effects of thermal annealing and chemical abrasion on ca. 3.5Ga metamict zircon and evidence for natural reverse discordance: Insights for UPb LA-ICP-MS dating. Chem. Geol. 466, 285-302. https://doi.org/https://doi.org/10.1016/j.chemgeo.2017.06.019.

Wilde, S.A., Valley, J.W., Peck, W.H., Graham, C.M., 2001. Evidence from detrital zircons for the existence of continental crust and oceans on the Earth 4.4 Gyr ago. Nature 409, 175-178. https://doi.org/doi:10.1038/35051550.

Williams, I.S., Compston, W., Black, L.P., Ireland, T.R., Foster, J.J., 1984. Unsupported radiogenic Pb in zircon: a cause of anomalously high Pb-Pb, U-Pb and Th-Pb ages. Contrib. Mineral. Petr. 88, 322-327.

Figure captions:

Fig. 1. Tera-Wasserburg concordia diagram showing the effect of Pb* mobilization on U-Pb dating of an ancient (e.g., 4300 Ma) zircon. (a) The effect of Pb* mobilization at different times. Generally, Pb* loss or enrichment leads to normal or reversely discordant data, respectively (e.g., line 1, t_2 = 2000 Ma). However, if Pb* mobilization occurred shortly after crystallization (e.g., line 2, t_2 = 3800 Ma), the data will intercept the concordia with typical precision for *in-situ* SIMS analysis (1% for $^{207}Pb/^{206}Pb$ and 2% for $^{206}Pb/^{238}U$, 2σ) until >50% Pb* enrichment, resulting in significantly older or younger apparently concordant ages. Each ellipse represents 10% Pb* loss or Pb* gain. t_1 and t_2 are the time of zircon crystallization and Pb* mobilization, respectively. The inset shows the definition of t_1 and t_2, as well as the $^{207}Pb/^{206}Pb$ ratio (I_0) of the Pb* formed between t_1 and t_2. (b) the effect of incorporating different numbers of Pb*-enriched domains (assuming 20 nm metallic Pb nanospheres, Kusiak et al., 2015) in a SIMS spot analysis (assuming a circular spot 20 μm in diameter and 0.1 μm in depth), using the equations in Ge et al (2018) and assuming t_2 = 3800 Ma and U = 30 ppm. The total number of metallic Pb nanosphere in this zircon (assuming a 180*120*120 μm ellipsoid) is estimated to be ~10^7 if all Pb* is present as metallic Pb, so even a very small portion of excess metallic Pb* would have a significant effect on U-Pb age.

Fig. 2. CL images showing internal structures and SHRIMP $^{207}Pb/^{206}Pb$ ages (±1σ, in Ma, %

discordance in brackets) of the studied Hadean zircon grains. (a) grain 14041; (b) grain 11085; (c) grain 12070; (d) grain 13015; (e) grain 14121; (f) grain 22026; (g) grain 23029; and (h) grain 22025. Dashed squares show the area studied using scanning ion imaging. Image 1 of grain 14041 in (a) is reported in Ge et al. (2018). Scale bar in all panels is 50 µm.

Fig. 3. CL, ^{238}U, ^{206}Pb and ^{207}Pb images showing the internal structures, distribution of U-Pb isotopes, and calculated ^{206}Pb/^{207}Pb ages for various regions of interest (ROIs) of the studied areas of the Hadean zircon grains. (a) grain 14041; (b) grain 11085; (c) grain 12070; (d) grain 13015; (e) grain 14121; (f) grain 22026; (g) grain 23029; and (h) grain 22025. Colour scale indicates relative counts/pixel intensity of the ions. Dashed lines in the ^{207}Pb images in the fourth panel indicate isotope profiles shown in Fig. 4. Ellipses and polygons in the last panel indicate different ROIs selected for age calculation (see text for details), where the numbers correspond to the number of ROIs and the calculated ^{207}Pb/^{206}Pb ages (in Ma) in Table S2. Note the first order control of the U, Th and Pb concentrations is by cracks, grain boundaries and CL zoning. Also note the presence of hotspots and patches of high ^{206}Pb and ^{207}Pb that do not correspond to high ^{238}U. These hotspots and patches correspond to different growth zones in different grains, as indicated by dotted areas in the CL images. They have exceptionally high apparent ^{207}Pb/^{206}Pb ages, and incorporating them into ~20 µm elliptical ROIs (similar to SIMS spot) results in spuriously older ^{207}Pb/^{206}Pb ages. Scale bar is 20 µm. Ion images of other isotopes can be found in Supplementary Fig. S1.

Fig. 4. Isotope profiles across the Pb* enriched domains (PEDs) showing ^{238}U, ^{206}Pb and ^{207}Pb counts (left axis) and ^{207}Pb/^{206}Pb ratios and ages (right axis). (a) grain 14041; (b) grain 11085; (c)

grain 12070; (d) grain 13015; (e) grain 14121; (f) grain 22026; (g) grain 23029; and (h) grain 22025. See Fig. 3 for locations of the profiles. Shaded bands indicate the PEDs. Note the high ^{207}Pb and ^{206}Pb in the core of grain 14041 are supported by high ^{238}U, but for the PEDs in this and other grains, the ^{207}Pb and ^{206}Pb peaks do not correspond to ^{238}U peaks, indicating ^{207}Pb and ^{206}Pb are not produced by *in-situ* U decay. Moreover, ^{207}Pb is more enriched than ^{206}Pb in these domains, producing extremely high ^{207}Pb/^{206}Pb ratios (up to 0.8 – 1.0) that correspond to apparent ages exceeding the age of the Earth, which indicates that the Pb* was concentrated in these domains shortly after crystallization.

Fig. 5. Tera-Wasserburg concordia diagrams showing the calculated ages (open ellipses) from the ion images compared to the SHRIMP data (filled ellipses). (a) grain 14041; (b) grain 11085; (c) grain 12070; (d) grain 13015; (e) grain 14121; (f) grain 22026; (g) grain 23029; and (h) grain 22025. Dashed lines are the discordia lines anchored at the estimated crystallization ages (see text for details) and fitted through the ion imaging and SHRIMP data, excluding outliers (dotted ellipses).

Fig. 6. A pseudo-3D reconstruction of a Pb*-enriched domain from grain 22025. Each layer represents an integration of 10 scans, which is estimated to represent ~0.5 – 1 nm in depth according to the depth profile study of Whitehouse et al. (2014). The intensity of ^{207}Pb increases and then decreases with increasing sputtering depth, suggesting a Pb*-enriched domain was fully traversed. This implies a vertical dimension of ~3 – 6 nm for the Pb*-enriched domain.

Table 2. Calculated α-dose for the studied Hadean zircon grains.

Grain no.	**14041**	**11085**	**12070**	**13015**	**14121**	**22026**	**23092**	**25025**
Crystallization age (t_1, in Ma)[a]	4300	4092	4029	4126	4189	4198	4182	4041
Pb* mobilization age (t_2, in Ma)[b]	3800	3500	3700	4100	3300	3600	4100	3300
U (ppm)[c]	28	134	151	80	76	138	218	156
Th (ppm)[c]	3	36	69	44	40	46	160	53
α dose at present ($\times 10^{15}$/mg)[d]	0.8	3.5	3.9	4.1	2.1	3.8	6.3	4.0
α dose at t_2 ($\times 10^{15}$/mg)[d]	0.2	0.9	0.6	0.1	0.8	1.0	0.3	1.2

Notes: [a]Best estimate from SHRIMP and/or ion imaging data; [b]Estimated from lower intercept ages in Fig. 6, except for grain 13015, for which a t2 value of ~4100 Ma is assumed (see text for explanation); [c]Representative U and Th contents of the domains related to Pb* mobilization; [d]α dose calculated using the equation in Murakami et al. (1991).

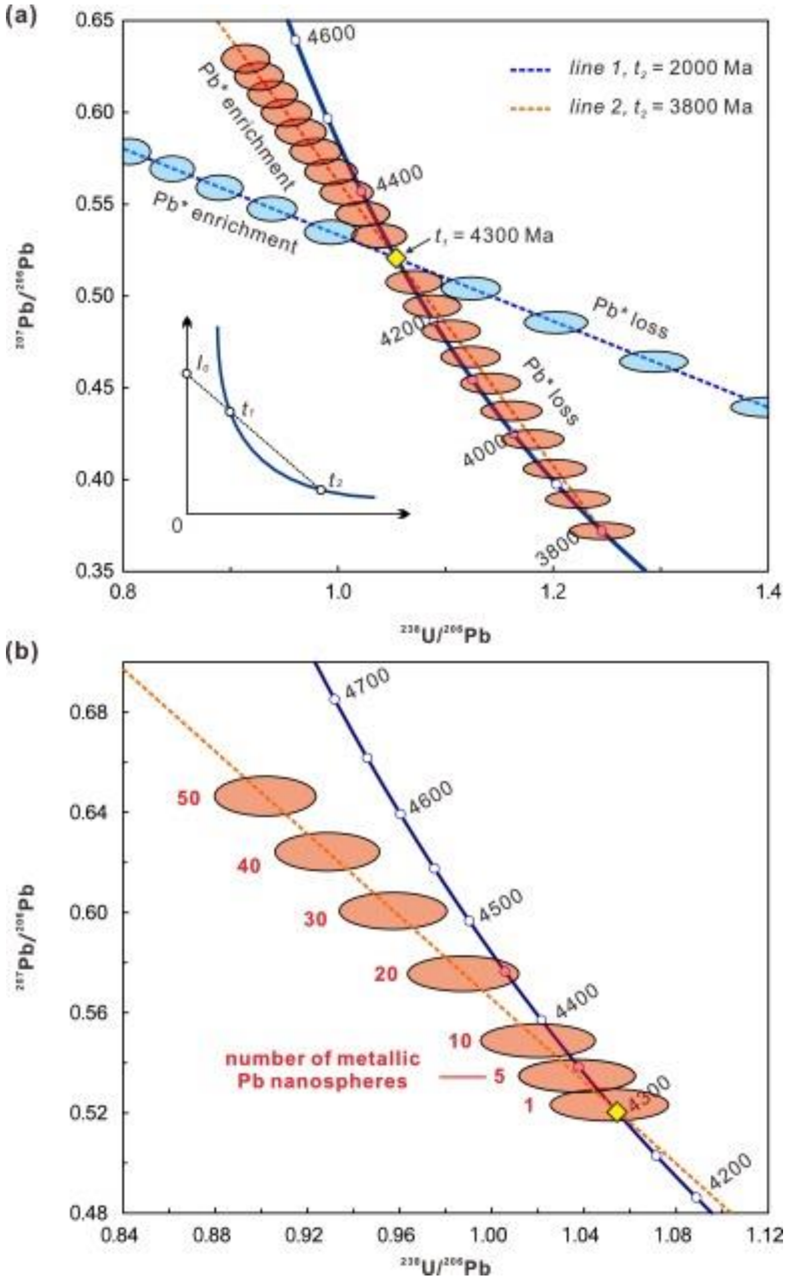

(a)
line 1, t_2 = 2000 Ma
line 2, t_2 = 3800 Ma
Pb* enrichment
Pb* enrichment
Pb* loss
Pb* loss
t_1 = 4300 Ma
4600
4400
4200
4000
3800
^{207}Pb/^{206}Pb
^{238}U/^{206}Pb
(b)
4700
4600
4500
4400
4300
4200
50
40
30
20
10
5
1
number of metallic
Pb nanospheres
^{207}Pb/^{206}Pb
^{238}U/^{206}Pb

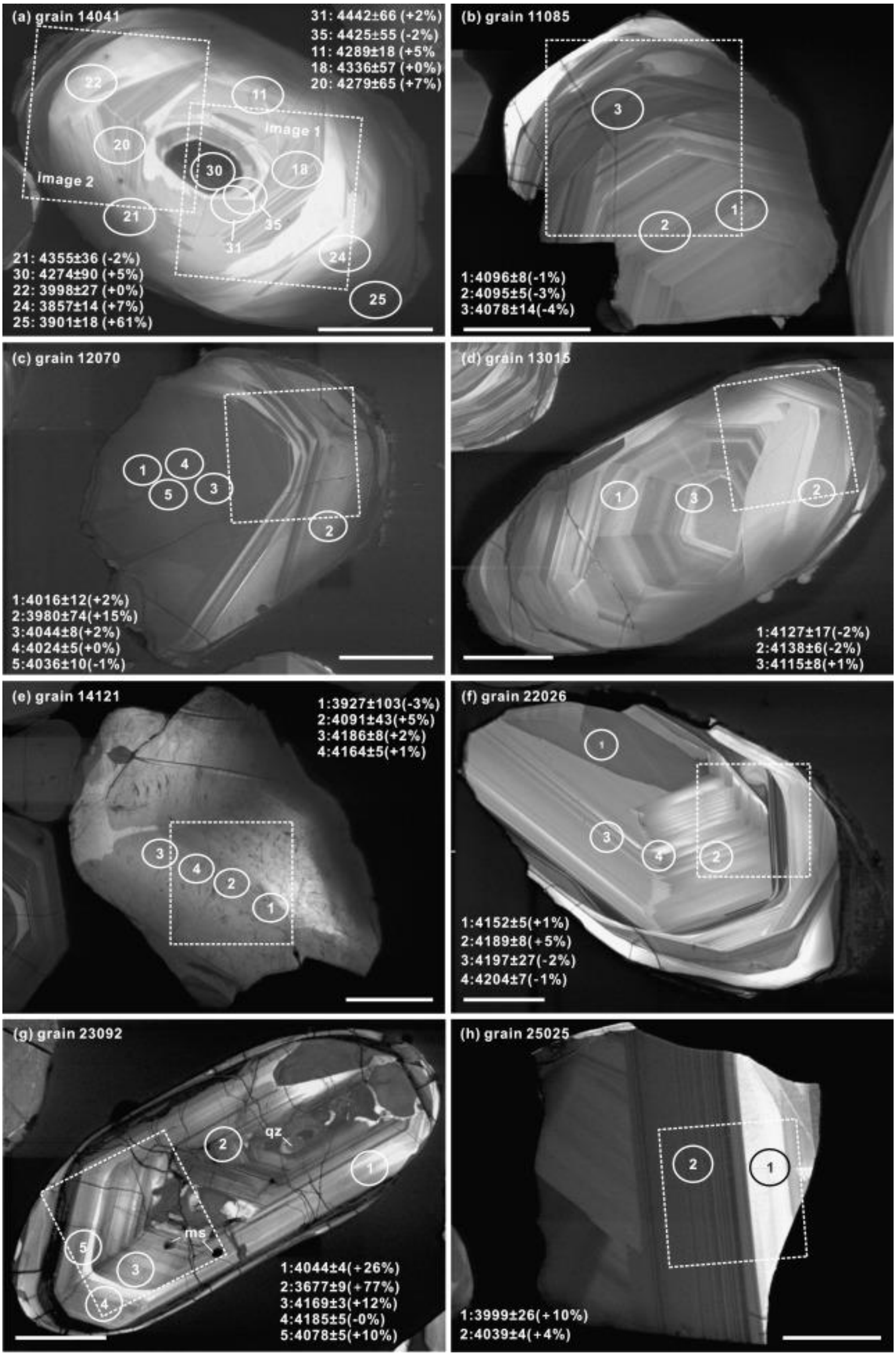
(a) grain 14041
31: 4442±66 (+2%)
35: 4425±55 (-2%)
11: 4289±18 (+5%
18: 4336±57 (+0%)
20: 4279±65 (+7%)
image 1
image 2
21: 4355±36 (-2%)
30: 4274±90 (+5%)
22: 3998±27 (+0%)
24: 3857±14 (+7%)
25: 3901±18 (+61%)
(b) grain 11085
1:4096±8(-1%)
2:4095±5(-3%)
3:4078±14(-4%)
(c) grain 12070
1:4016±12(+2%)
2:3980±74(+15%)
3:4044±8(+2%)
4:4024±5(+0%)
5:4036±10(-1%)
(d) grain 13015
1:4127±17(-2%)
2:4138±6(-2%)
3:4115±8(+1%)
(e) grain 14121
1:3927±103(-3%)
2:4091±43(+5%)
3:4186±8(+2%)
4:4164±5(+1%)
(f) grain 22026
1:4152±5(+1%)
2:4189±8(+5%)
3:4197±27(-2%)
4:4204±7(-1%)
(g) grain 23092
qz
ms
1:4044±4(+26%)
2:3677±9(+77%)
3:4169±3(+12%)
4:4185±5(-0%)
5:4078±5(+10%)
(h) grain 25025
1:3999±26(+10%)
2:4039±4(+4%)

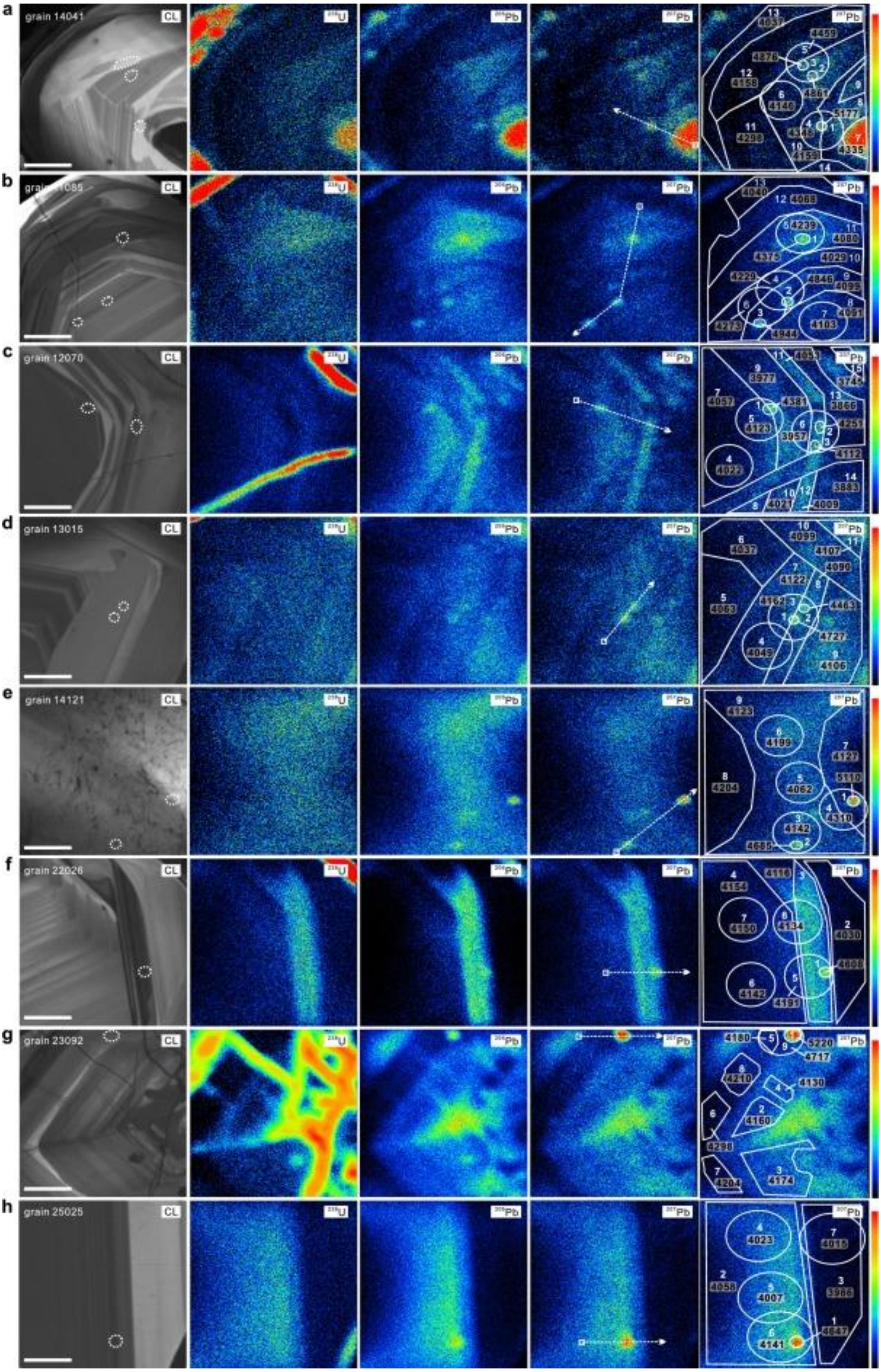
a
grain 14041
CL
b
CL
c
grain 12070
CL
d
grain 13015
CL
e
grain 14121
CL
f
grain 22026
CL
g
grain 23092
CL
h
grain 25025
CL

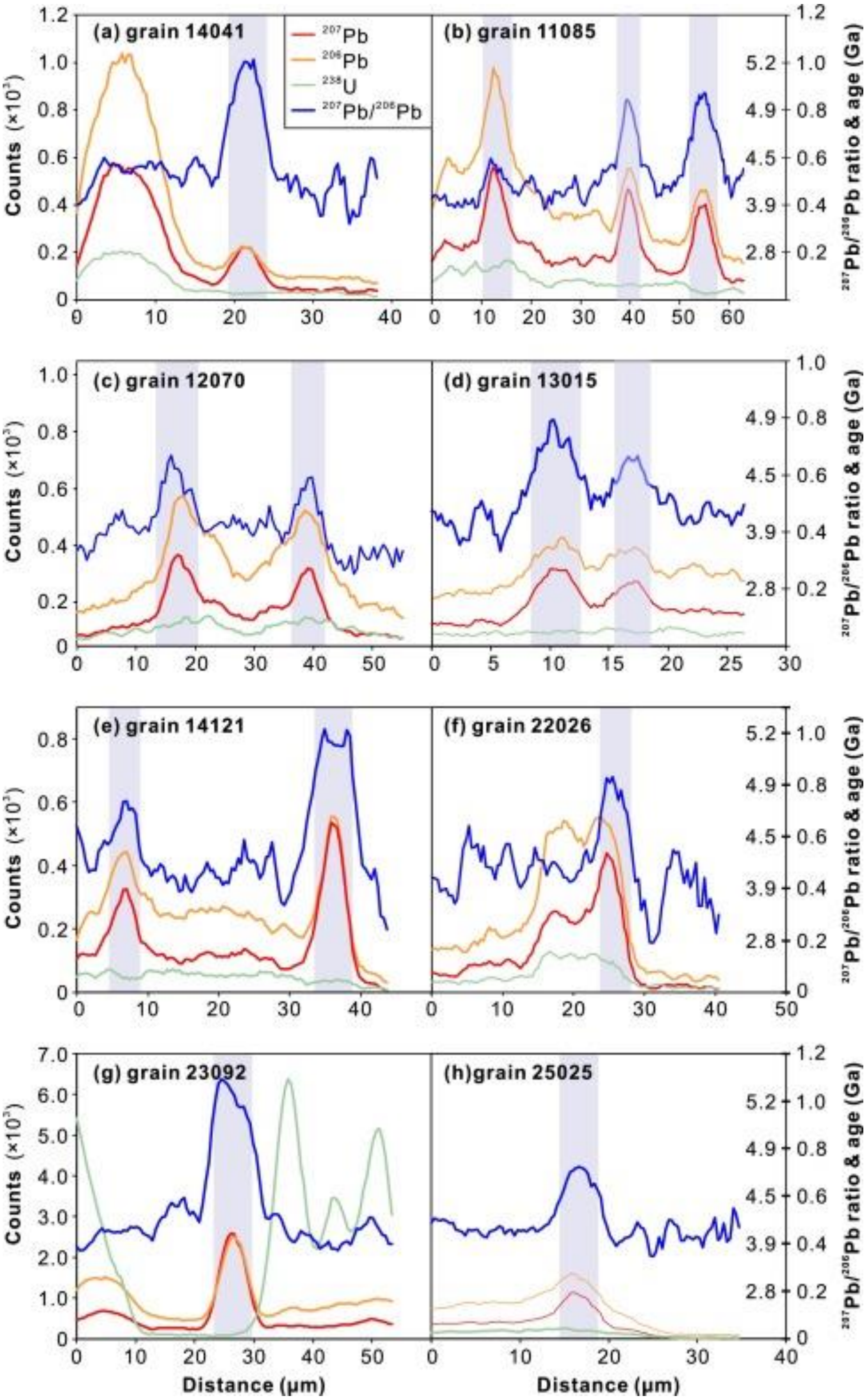
(a) grain 14041
(b) grain 11085
(c) grain 12070
(d) grain 13015
(e) grain 14121
(f) grain 22026
(g) grain 23092
(h)grain 25025
207Pb
206Pb
238U
207Pb/206Pb
Counts (×10³)
207Pb/206Pb ratio & age (Ga)
Distance (μm)

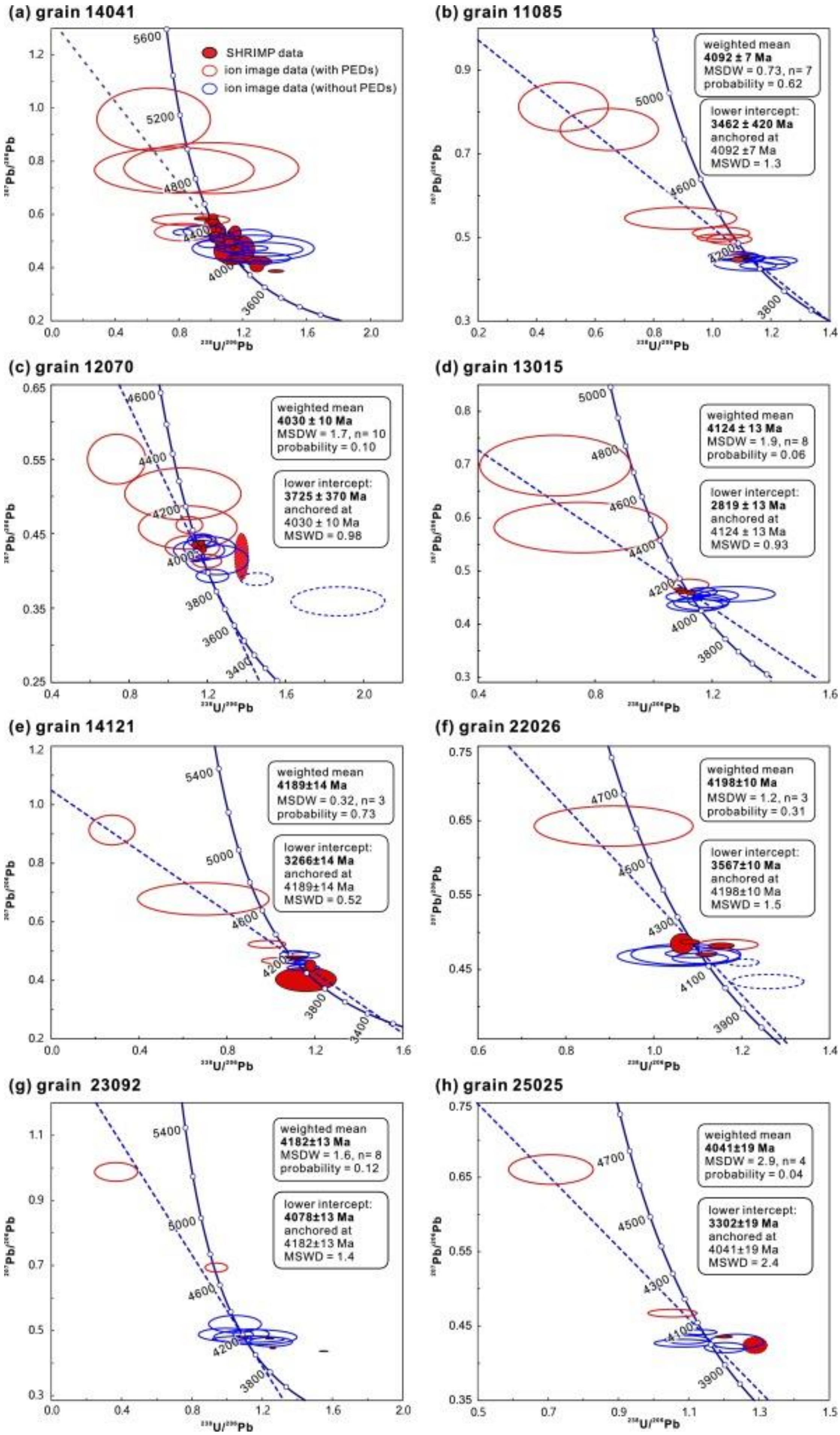
(a) grain 14041
SHRIMP data
ion image data (with PEDs)
ion image data (without PEDs)
(b) grain 11085
weighted mean
4092 ± 7 Ma
MSDW = 0.73, n= 7
probability = 0.62
lower intercept:
3462 ± 420 Ma
anchored at
4092 ±7 Ma
MSWD = 1.3
(c) grain 12070
weighted mean
4030 ± 10 Ma
MSDW = 1.7, n= 10
probability = 0.10
lower intercept:
3725 ± 370 Ma
anchored at
4030 ± 10 Ma
MSWD = 0.98
(d) grain 13015
weighted mean
4124 ± 13 Ma
MSDW = 1.9, n= 8
probability = 0.06
lower intercept:
2819 ± 13 Ma
anchored at
4124 ± 13 Ma
MSWD = 0.93
(e) grain 14121
weighted mean
4189±14 Ma
MSDW = 0.32, n= 3
probability = 0.73
lower intercept:
3266±14 Ma
anchored at
4189±14 Ma
MSWD = 0.52
(f) grain 22026
weighted mean
4198±10 Ma
MSDW = 1.2, n= 3
probability = 0.31
lower intercept:
3567±10 Ma
anchored at
4198±10 Ma
MSWD = 1.5
(g) grain 23092
weighted mean
4182±13 Ma
MSDW = 1.6, n= 8
probability = 0.12
lower intercept:
4078±13 Ma
anchored at
4182±13 Ma
MSWD = 1.4
(h) grain 25025
weighted mean
4041±19 Ma
MSDW = 2.9, n= 4
probability = 0.04
lower intercept:
3302±19 Ma
anchored at
4041±19 Ma
MSWD = 2.4
207Pb/206Pb
238U/206Pb

746